Investigation of nucleation processes during dynamic recrystallization of ice using cryo-EBSD

T. Chauve, M. Montagnat, Fabrice Barou, K. Hidas, Andrea Tommasi, David Mainprice

PHILOSOPHICAL TRANSACTIONS A

rsta.royalsocietypublishing.org

Research

Cite this article: Chauve T, Montagnat M, Barou F, Hidas K, Tommasi A, Mainprice D. 2017 Investigation of nucleation processes during dynamic recrystallization of ice using cryo-EBSD. *Phil. Trans. R. Soc. A* **375**: 20150345. http://dx.doi.org/10.1098/rsta.2015.0345

Accepted: 17 June 2016

One contribution of 11 to a theme issue 'Microdynamics of ice'.

Subject Areas:
glaciology, materials science

Keywords:
dynamic recrystallization, nucleation, electron backscatter diffraction, ice

Author for correspondence:
M. Montagnat
e-mail: maurine.montagnat@univ-grenoble-alpes.fr

Electronic supplementary material is available online at https://dx.doi.org/10.6084/m9.figshare.c.3579809.

THE ROYAL SOCIETY PUBLISHING

Investigation of nucleation processes during dynamic recrystallization of ice using cryo-EBSD

T. Chauve[1], M. Montagnat[1], F. Barou[2], K. Hidas[2], A. Tommasi[2] and D. Mainprice[2]

[1]Univ. Grenoble Alpes, CNRS, IGE (LGGE), F-38000 Grenoble, France
[2]Geosciences Montpellier, Université Montpellier 2 — CNRS, France

TC, 0000-0003-2916-7472; MM, 0000-0001-9436-5163

Nucleation mechanisms occurring during dynamic recrystallization play a crucial role in the evolution of microstructures and textures during high temperature deformation. In polycrystalline ice, the strong viscoplastic anisotropy induces high strain heterogeneities between grains which control the recrystallization mechanisms. Here, we study the nucleation mechanisms occurring during creep tests performed on polycrystalline columnar ice at high temperature and stress ($T = -5°C; \sigma = 0.5$ MPa) by post-mortem analyses of deformation microstructures using cryogenic electron backscatter diffraction. The columnar geometry of the samples enables discrimination of the nuclei from the initial grains. Various nucleation mechanisms are deduced from the analysis of the nuclei relations with the dislocation sub-structures within grains and at grain boundaries. Tilt sub-grain boundaries and kink bands are the main structures responsible for development of polygonization and mosaic sub-structures. Nucleation by bulging at serrated grain boundaries is also an efficient nucleation mechanism near the grain boundaries where strain incompatibilities are high. Observation of nuclei with orientations not related to the 'parent' ones suggests the possibility of 'spontaneous' nucleation driven by the relaxation of the dislocation-related internal stress field. The complexity of the nucleation mechanisms

observed here emphasizes the impact of stress and strain heterogeneities on dynamic recrystallization mechanisms.

This article is part of the themed issue 'Microdynamics of ice'.

1. Introduction

Understanding ice deformation behaviour is a key point for ice flow modelling and interpretation of climatic signals extracted from ice cores. Ice has a hexagonal crystallographic structure, where the [0001] direction is called the optical axis or *c*-axis. Deformation in ice occurs mainly by dislocation glide in the basal plane, that is, in the plane normal to the *c*-axis, conferring a strong viscoplastic anisotropy to the crystal [1,2]. The strong strain heterogeneity that ensues from this anisotropy results in activation of dynamic recrystallization even at very low strains (less than or equal to 1% in laboratory conditions) [3]. Dynamic recrystallization processes in ice are similar to those observed in rocks and metals [4,5].

During deformation within an ice sheet, various recrystallization processes occur [6]. They modify the ice texture and microstructure [7,8], and therefore affect the flow behaviour [9–11]. From texture analyses along deep ice cores, it is suggested that continuous (or rotation) dynamic recrystallization (continuous DRX) predominates at intermediate depths [12,13], whereas discontinuous (or migration) dynamic recrystallization (discontinuous DRX) prevails at deeper depths, close to the base of the ice sheet where deviatoric stress and temperature are higher [6,12,14]. These two dynamic recrystallization regimes produce different microstructures and distribution of crystallographic orientations (textures). When continuous DRX is dominant, ice subjected to a very low vertical compressive stress (which is the most common stress field along ice cores drilled at geological domes, except close to the bedrock) develops a texture characterized by *c*-axes forming a single maximum aligned with the compression direction. This texture evolution is well explained by the rotation of basal planes driven by dislocation glide and is probably only slowed down by continuous DRX mechanisms [7,15,16]. When discontinuous DRX is the dominant mechanism, the texture evolves toward an arrangement of *c*-axes within small circles oriented at about 35° from the compression axis [6,8,17]. The latter texture is also obtained in laboratory compressive creep experiments performed at higher homologous temperatures, but under deviatoric stresses 3–10 times larger than expected in an ice sheet [18,19].

Both recrystallization regimes are driven by a redistribution of stored strain energy, associated with the dislocations via grain boundary migration and nucleation of strain free grains. The exact mechanisms responsible for the development of a given texture, in particular during discontinuous DRX, are still questioned. In particular, the interaction between local heterogeneities in the strain field, DRX mechanisms and the role of nucleation in texture development, under laboratory conditions or in ice sheets are still poorly constrained.

Development of strain heterogeneities in ice has been characterized at an intragranular scale (and relatively high resolution) by Grennerat *et al.* [20]. They showed that strain tends to concentrate close to grain boundaries and sub-grain boundaries (SGBs) in relation to the stress field heterogeneities [21,22]. Recent strain field measurements performed at a triple junction where nucleation occurred [3] showed that DRX mechanisms initiate where strain incompatibilities between neighbouring grains are strong and that the change in the microstructure tends to relax the incompatibilities. Duval *et al.* [23] proposed a strong connection between nucleation and local internal stress field resulting from dislocation arrangements. The role of dislocation accumulation and arrangement under heterogeneous strain fields appears to be crucial for DRX processes.

Dislocations responsible for plastic deformation in ice have their Burgers vector dominantly along one of the $\langle a \rangle$ ($\langle 1\bar{1}20 \rangle$) axis and glide in the basal plane [2,24]. Very short segments of non-basal $\langle a \rangle$ dislocations were observed by X-ray diffraction [25–27]. Being rare, non-basal dislocations are usually assumed not to significantly contribute to the deformation, but they are

supposed to participate in the generation of basal dislocations [28]. Recent analysis of electron backscatter diffraction (EBSD) data on ice [22,29] showed that non-basal $\langle c \rangle$ or $\langle c + a \rangle$ dislocations contribute to some of the observed SGB structures.

The most common sub-structures in both naturally and experimentally deformed ice polycrystals are tilt SGBs or kink bands composed of basal edge dislocations [22,30,31]. Kink bands are characterized by a combination of two opposite tilt SGBs [32,33]. They may be viewed as equivalent to twinning that frequently occurs in hexagonal or trigonal materials such as magnesium [34,35], titanium [36] or calcite [37] because both structures can accommodate local shear in a 'hard slip' direction [3,22,38]. These SGBs and kink bands modify the texture and microstructure in a similar way as observed during continuous DRX in metals [39,40] and rocks [41–43].

Strain heterogeneity also results in strain induced grain boundary migration (SIBM), which results in serrated (or interlobate) grain boundaries, commonly observed in ice and also metals and rocks [41,44–47]. Grain boundary bulging resulting from SIBM has often been suggested as a likely nucleation mechanism in ice [6,19,31,48].

In this study, we discuss nucleation mechanisms in ice based on post-mortem observations of microstructures on columnar ice polycrystals deformed in the laboratory. Tests were performed under creep at high temperature and relatively high deviatoric compressive stresses ($T \approx -7^{\circ}$C and $\sigma = 0.5$ MPa). The polycrystalline columnar ice microstructure with large grains (1–2 cm diameter) enables relatively high resolution observations for ice (down to 5 µm) of nuclei, sub-grain and grain boundary structures by cryogenic EBSD (cryo-EBSD), which provides the full crystallographic orientation of grains. In addition, this study tries to unravel the likely nature of the dislocations involved in these structures, aiming to improve our understanding of the connection between strain heterogeneities, nucleation mechanisms and textures.

We keep in mind, as highlighted by Humphreys & Hatherly [49], that when observing nucleation, one is in fact studying *nucleation and the early stage of growth* because nucleation is a part of recrystallization process which is well below the resolution limit of instruments used for this investigation.

2. Experimental set-up

(a) Creep tests on polycrystalline columnar ice

Creep tests were performed in uniaxial compression in a cold room at -7°C ($\pm 0.5^{\circ}$C). A constant stress of 0.5 MPa was applied through a constant load along the vertical y-axis. Under these conditions, a minimum strain rate of about $3 \times 10^{-7}\,\mathrm{s}^{-1}$ is reached at 1% strain, after about 3 h. Teflon sheets were placed between the sample and the pistons in order to minimize friction at the contact surfaces, which could induce shear. As the macroscopic strain reached less than 3%, we neglected the evolution of the surface in contact with the load. Tests were stopped at low macroscopic strains (around 3%) to focus on the initial stages of recrystallization, in particular nucleation.

The samples were made of columnar polycrystalline ice of type S2 [50]. The columns are nearly parallel to each other and the initial orientation of the c-axis of the grains is within $\pm 15^{\circ}$ from the plane perpendicular to the columns. Samples were machined in the laboratory with high geometrical accuracy to a parallelepiped shape of dimensions close to $85 \times 85 \times 15\,\mathrm{mm}^3$, with the shortest direction being parallel to the columns of the grains. The microstructure of a non-deformed sample, in the plane perpendicular to the columns, is shown in figure 1. The typical size of the grains in this plane is about 1–2 cm, and each sample is composed of about 80 grains. Texture analysis techniques used here are mostly destructive (see §2b) but the 2.5-dimensional geometry of the sample provided by the columnar microstructure enables one to compare pre- and post-deformation textures and microstructures by preparing sub-parallel samples along the plane perpendicular to the column axes. The columnar geometry also allows discriminating without ambiguity new recrystallized small grains from large parent grains (figure 1).

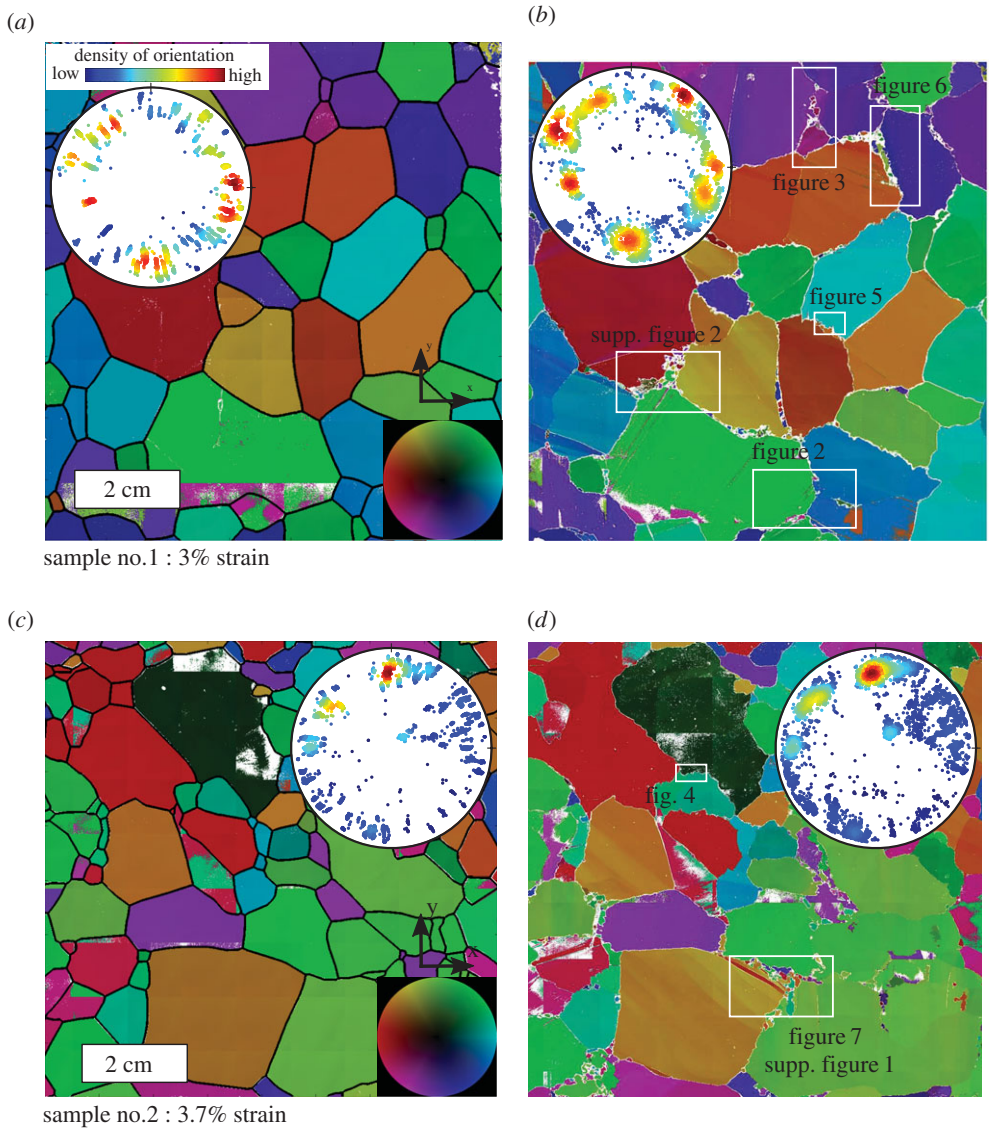

Figure 1. Pre- (*a,c*) and post- (*b,d*) deformation texture analyses from [0001] *c*-axis measurements performed with the AITA (20 µm step size), with the associated pole figure for [0001] axis for both sample no. 1 (*a,b*) and no. 2 (*c,d*). The colourwheel related to *c*-axis orientations is shown at the bottom right of the undeformed microstructures. Selected areas for EBSD analyses are shown within white rectangles on the deformed microstructures. The white pixels in post-deformation microstructures are non-indexed. (Online version in colour.)

For a more detailed description of the creep test conditions and sample fabrication the reader can refer to [3,20].

(b) Texture and microstructure analyses

The automatic ice texture analyzer (AITA) [51] provides measurements of the orientation of the optical *c*-axis over large areas with a spatial step size varying between 50 and 5 µm (we use 20 µm here) and an angular resolution of about 3° [52]. The *c*-axis measurement is more sensitive to the colatitude angle, this explains the radial dispersion visible on the pole figure for the undeformed sample, which provides the range of accuracy. Measurements are performed on

a thin section (0.3 mm thick) of the full sample area ($85 \times 85\,mm^2$) extracted before the test and on a section cut on the sample surface just after the test, as close as possible to the previous one [20] (figure 1). The distance between the two thin sections is estimated to be around 5 mm. Owing to the columnar shape of the grains and their large diameter, we expect limited bias from two-dimensional sectioning.

Cryo-EBSD analyses are performed over small areas of interest ($2 \times 1\,cm^2$) selected based on the AITA observations. We used the crystal probe scanning electron microscope of Geosciences Montpellier (CNRS, Université Montpellier 2) mounted with a GATAN cold stage module as described in [19]. The full lattice orientation is obtained with a step size between 50 and 0.1 µm and an angular resolution of 0.7° [53]. Appropriate adjustment of the vacuum and temperature (1 Pa and −100°C) to reduce sublimation was made following Weikusat *et al.* [54] and allowed EBSD mapping of the entire selected areas ($2 \times 1\,cm^2$) with indexation rates higher than 85%. Samples for EBSD analyses were extracted as close as possible to the sample surface, at about 6 mm behind the thin section analysed with the AITA. Microstructures derived from the two orientation mapping techniques compare remarkably well (figure 1).

Analyses of post-deformation texture by the AITA were performed at −15°C immediately at the end of the tests. Samples were later maintained at −40°C, transported at −18°C (a few hours) and prepared at −60°C prior to EBSD observations to limit the effect of post-dynamic recrystallization or annealing.

(c) Characterization tools for the interpretation of EBSD data

EBSD data treatment was performed using the MTEX open source Matlab toolbox (http://mtex-toolbox.github.io/) [55]. Definitions of some parameters implemented in MTEX and used for the study are given in this section.

Grain segmentation was done with a transition angle from sub-grain boundary to grain boundary fixed at 7°. The relevance of this value is discussed in the electronic supplementary material by comparing the measured grain boundary energy [56,57] with theoretical SGB energy using the Read and Shockley model [58].

Mis2mean computes for each pixel the misorientation, i.e. the minimum rotation angle, between the pixel orientation and the mean orientation of the grain. Maps of the mis2mean values are used to illustrate intragranular misorientations associated with SGBs.

GOS, the grain orientation spread, is the mean value of mis2mean within a grain. The GOS value provides a scalar magnitude of the global misorientation inside the grain.

KAM, the kernel average misorientation, is a measurement of the local misorientation. It is calculated as the average misorientation angle between a pixel and its neighbours. In this study, 12 neighbouring pixels are used for the calculation (second order KAM). Maps of the KAM are used to highlight areas of abrupt changes in orientation, such as SGBs.

Misorientation profiles are used to characterize sub-structures such as SGBs and kink bands. Two types of misorientation profiles were calculated. The first type plots the misorientation between a pixel along a selected profile, and the first pixel in the profile (red line). The second type plots the misorientation between two adjacent pixels along the profile (blue line). When relevant, a pole figure showing the rotation axis of the misorientation accommodated by a SGB that crosscuts the profile is also displayed.

The **misorientation axis** is extracted by measuring the change in crystal orientation across a SGB, following the technique suggested in [59]. As we force the misorientation angle to be positive, two rotations in opposite sense will have the same misorientation angle but misorientation axes pointing in opposite directions, hence in opposite hemispheres. The rotation axis is therefore represented in the hemisphere in which it is pointing.

In order to interpret the nature of the SGB (tilt or twist), the orientation of the SGB plane is also required. This information cannot be extracted from the EBSD data, which only provides the trace of this plane on the sample surface. The assumption made to define the SGB plane needs to be justified in each case [22,30].

3. Nucleation processes

Pre- and post-deformation textures and microstructures obtained using the AITA are shown in figure 1 together with pole figures displaying the orientations of the *c*-axes. Owing to the initial centimetre size columnar microstructure, we are able to discriminate small grains at grain boundaries and triple junctions as being nuclei formed by DRX. Many dislocation sub-structures, forming SGBs are observed, and grain boundaries are highly serrated.

The texture is not significantly modified relative to the starting material because the orientations of the large initial grains still dominate the final texture. Texture in the deformed samples is more dispersed due to onset of nucleation and development of intragranular misorientations.

Specific areas were selected on the deformed samples based on the AITA images and analysed by EBSD (white rectangles in figure 1). EBSD analyses enable one to characterize local features from the full crystallographic orientations, and at relatively high resolution (20–5 µm) relative to the grain size. These features are presented below based on the nucleation mechanism we assumed they record, namely polygonization by SGB formation or nucleation at grain boundaries and triple junctions.

(a) Polygonization

Polygonization involves the formation of SGBs that can further evolve with strain into new grain boundaries and create new grains. In the configuration of post-mortem observations, we only observe SGBs and cannot predict their evolution into new grain boundaries. We observe different types of SGBs that we characterize by using the tools described in §2c from cryo-EBSD data.

(i) Tilt sub-grain boundaries and kink band structures

Tilt SGBs are the most commonly observed sub-structures in our experiments or in previous studies [21,29,30]. They are composed of edge dislocations [60]. Some well-defined tilt SGBs are illustrated in part 1 of the electronic supplementary material. They appear either as individual structures crossing the entire grain, or as multiple tilt SGBs that bend grains up to high misorientations (up to 8° in the given example).

A kink band is a special arrangement of two parallel tilt SGBs with opposite misorientation axis directions, each tilt SGB inducing the same absolute angle of misorientation. Hence, at both sides of the kink band the crystal orientation is nearly identical. Many kink bands are observed in our samples. A few are described here. A large kink band is shown in figure 2, crosscutting grain P6. The KAM representation used in this figure highlights the regions of abrupt changes in orientation. The tilt nature of the two SGBs forming the kink band is determined by using the misorientation axis analysis described in §2c.

The pole figure (figure 2) shows that the misorientation axes are parallel to a ⟨*a*⟩ axis for the right SGB and to a ⟨*m*⟩ axis for the left one. Both rotation axes are in the basal plane. Such tilt SGBs were characterized in [22]. They are interpreted as tilt walls based on the assumption that the sub-grain wall is almost perpendicular to the sample surface. Although this assumption is reasonable given the columnar geometry of the samples, only three-dimensional measurements could confirm it. Based on this assumption, the ⟨*c*⟩ axis lies within the SGB plane, hence these SGBs are tilt SGBs essentially made of basal edge dislocations with ⟨*a*⟩ Burgers vectors.

The misorientation profile (figure 2*b*) shows that both tilt SGBs accommodate a total misorientation close to 3°. However, in both SGBs, the misorientation between two adjacent pixels is never higher than 1° (cf. the blue curve in figure 2*b*). The change in orientation across the two tilt SGBs that form this kink band is not a sharp step but a progressive misorientation. Such a 'smooth' misorientation gradient is rarely observed in tilt SGBs. Most tilt SGBs analysed in this study show sharp misorientation gradients.

Kink band arrangements are often observed to crosscut the entire grain, but some of them, which initiate close to a grain boundary, tend to vanish in the grain interior. An illustration is

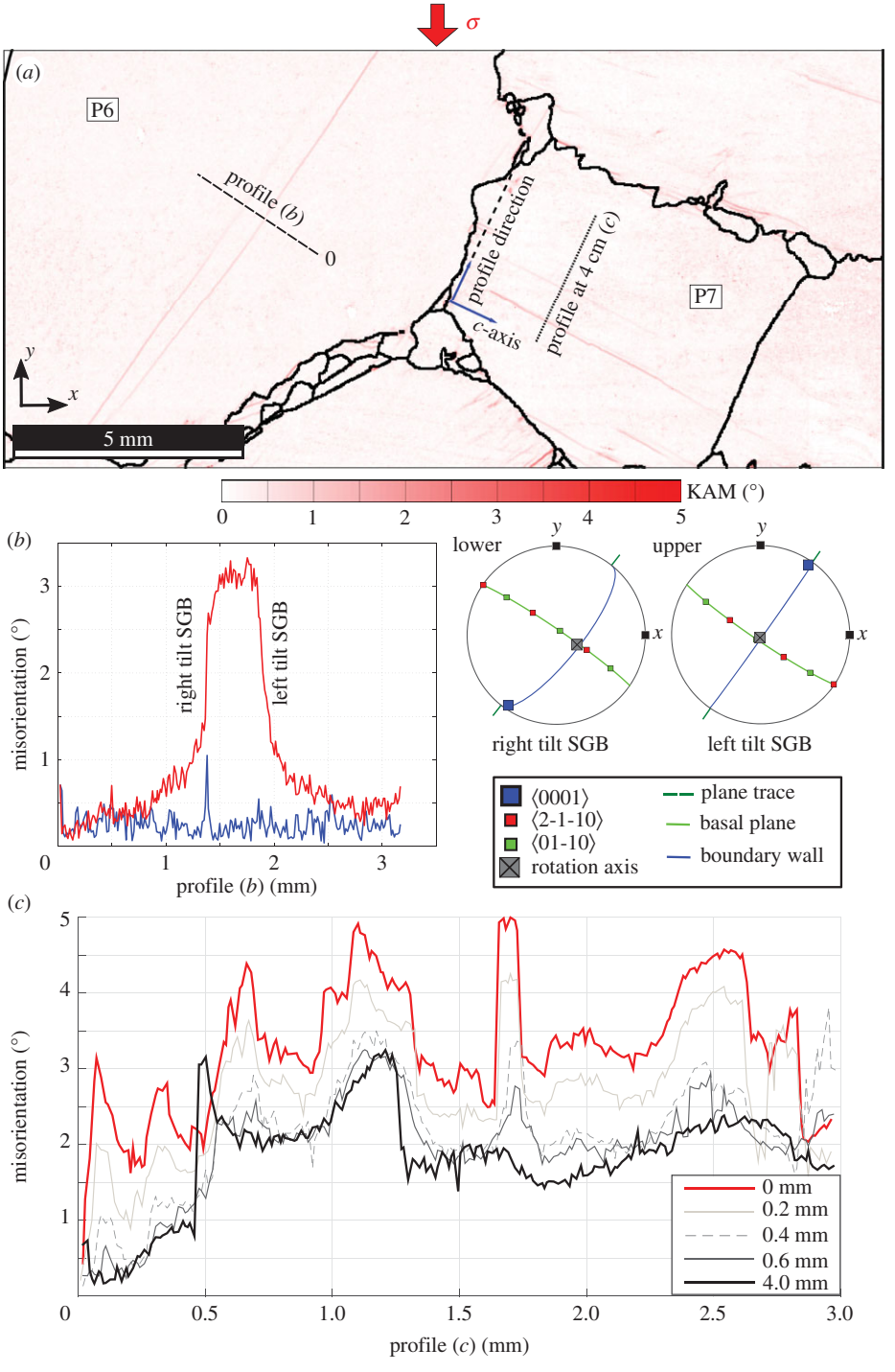

Figure 2. (*a*) KAM representation of an EBSD map (20 µm step size). The grain boundaries are plotted in black (misorientation angle higher than 7°). (*b*) Misorientation angle analysis along profile (*b*); the red line shows the cumulative misorientation and the blue line the misorientation between neighbouring pixels, associated pole figures for the right and left tilt SGB pointing in different hemispheres. (*c*) Misorientation angle evolution along various profiles across grain P7, at increasing distances from the grain boundary. Profiles are extracted perpendicularly to the *c*-axis direction, in order to show the sub-structure evolution as a function of the distance to the grain boundary. (Online version in colour.)

given in figure 2, where several misorientation profiles are extracted along parallel lines taken at increasing distances from the grain boundary between grains P6 and P7. The red profile plotted in figure 2*c* (labelled '0.0 mm') corresponds to the profile closest to the grain boundary. The black profile is the furthest away from the boundary. While many kink band structures, of various widths, are present close to the grain boundary, only a few remain 4 mm away from the grain boundary. For instance, the kink band visible at about 1.7 to 1.8 mm along the red profile is no longer detected in the grain interior and does not appear on the black profile. In addition, the complex sub-structure that appears between about 0.5 and 1.4 mm along the red profile tends to concentrate, or organize itself, in the shape of a wide kink band visible along the black profile (and visible in the KAM representation of figure 2). These observations show that close to grain boundaries more kink bands and tilt SGBs are produced, probably due to strain incompatibilities between neighbouring grains with very different orientations.

(ii) Mosaic sub-structures

Both tilt SGB and kink band structures observed here are assumed to be made of a simple configuration of basal edge dislocations, similar to previous descriptions in [30]. KAM representations of EBSD data also highlight areas with more complex sub-structures, including curved SGBs, often close to grain boundaries and triple junctions.

A typical SGB structure of this type appears in grain P8 (figure 3), where SGBs split a parent grain in three sub-grains. These three SGBs are coherent with tilt SGBs, following the reasoning of §3a(i). The three misorientation axes are between $\langle a \rangle$ and $\langle m \rangle$ axes (figure 3*b*). Interestingly, the misorientation axis resulting from the combination of SGB P8-S1 and SGB P8-S2 (grey square, figure 3*b*) is similar to the one created by SGB P8-S3. The resulting misorientation angle is slightly different, the combination of SGB P8-S1 and SGB P8-S2 resulting in a rotation of 8.4° while SGB P8-S3 creates a rotation of 9.4°. This difference is explained by an additional progressive misorientation gradient, which can be observed along a profile following SGBs P8-S1 and P8-S3 (figure 3*a*).

(b) Nucleation at triple junctions and along grain boundaries

(i) Serrated grain boundaries and nucleation by bulging

EBSD maps obtained at 5 µm steps show that most grain boundaries are highly serrated after the 3% strain reached at the end of the compressive creep test (figure 4). These serrated grain boundaries result from grain boundary migration driven by local variations in dislocation density between two neighbouring grains [49,61]. In the vicinity of serrated grain boundaries, the grains often display strongly misoriented domains (up to 5°, figure 4) where SGBs form complex structures. In the following, we will analyse some of these sub-structures. The mis2mean representation is chosen in order to highlight the sub-grains rather than their boundaries.

Figure 4 shows a typical serrated grain boundary structure where various SGBs appear at the edges of the bulged part of the grain boundary. Analysis of SGBs P10-S1, P10-S2 and P9-S1 (figure 4) illustrates the complexity of the dislocation sub-structure in such domains.

The misorientation axes are between $\langle a \rangle$ and $\langle m \rangle$ directions in the basal plane for the three SGBs P10-S1, P10-S2 and P9-S1. All these SGBs have a typical tilt boundary geometry with the misorientation axis in the boundary plane. In the case of P10-S2, the boundary wall is perpendicular to the *c*-axis. By making the hypothesis that the SGB plane is perpendicular to the plane of the section, this SGB can be interpreted as composed by non-basal $\langle c \rangle$ dislocations, such as hypothesized in [22,29].

In order to create new grains from bulging, one needs these SGBs to turn into grain boundaries and separate the bulged area from the parent grain. Once again, post-mortem analyses such as those performed here can only provide indirect observations of such a mechanism. Some nuclei, assumed to have formed by this process along a serrated grain boundary are shown in figure 5. In this figure, the mis2mean representation indicates a high density of dislocation sub-structures

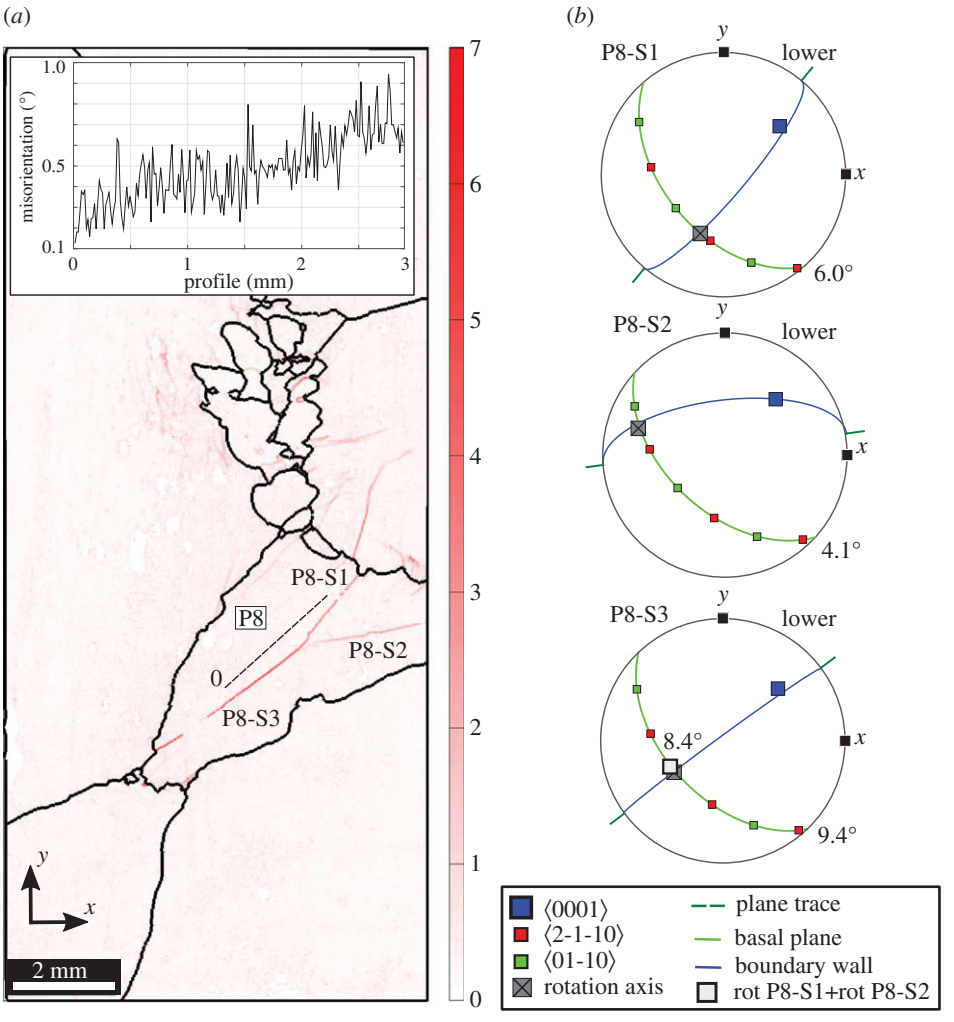

Figure 3. (*a*) Second order KAM of an EBSD map showing mosaic sub-structure (20 μm step size). The profile shows the cumulative misorientation along the dashed line relative to labelled point 0. The grain boundaries are plotted in black (misorientation angle higher than 7°). (*b*) Pole figures for each SGB. The total misorientation accommodated by the SGB is indicated at the bottom right of the pole figure. On the SGB P8-S3 pole figure, the misorientation axis resulting from the combination of the misorientations of SGBs P8-S1 and P8-S2 is plotted as a grey square. (Online version in colour.)

within the parent grain P12 which results in a high GOS for this grain. On the contrary, the GOS of the small grains n1 and n2 is low and very low mis2mean values are measured in these grains. Based on the smooth shape of grain boundaries between grain n1 and grain P12, and between grain n2 and grain P12, we assume the two small grains to have grown at the expense of grain P12. This interpretation is substantiated by the fact that the mis2mean map shows more sub-structures in the vicinity of the small grains within grain P12 than within grain P11.

The pole figure shown in figure 5 represents the orientation of each grain of the figure, with symbols proportional to the grain size. The orientations of the small grains n1 and n2 are close to the orientation of grain P11, while the orientation of the small grain r1 is close to grain P12. Grain r1 is also characterized by a high GOS value and has a relatively serrated grain boundary. Based on these observations, we hypothesize that n1 and n2 are new grains formed by bulging of the grain boundary between P11 and growing at the expense of P12, while grain r1 could well be a

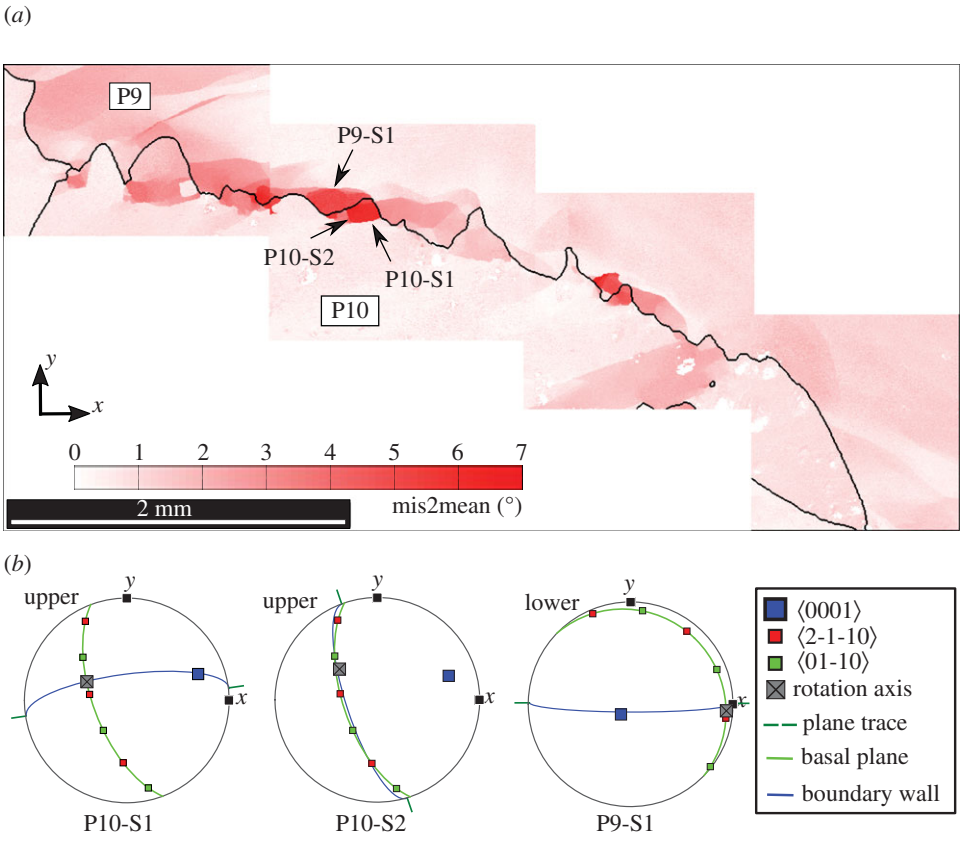

Figure 4. (*a*) Mis2mean representation of a serrated grain boundary from an EBSD map (5 µm step size). The grain boundaries are plotted in black (misorientation angle higher than 7°). (*b*) Pole figures for SGB analyses are plotted for P9-S1, P10-S1 and P10-S2. (Online version in colour.)

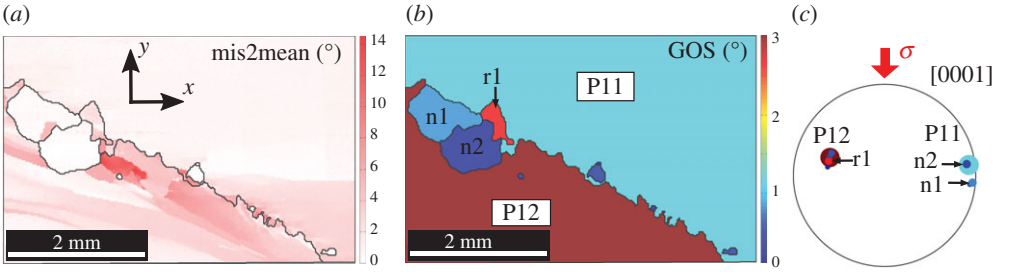

Figure 5. EBSD map (20 µm step size) of serrated GB with nuclei. The grain boundaries are plotted in black (misorientation angle higher than 7°). (*a*) Mis2mean representation. (*b*) GOS magnitude map colour-coding. (*c*) *c*-Axis ⟨0001⟩ pole figure using the GOS colourcode and a maker size proportional to the grain size. (Online version in colour.)

small part of grain P12 isolated by the nucleation and growth of n1 and n2. We may call grain r1 a remnant of grain P12.

Nucleation by bulging creates new grains with low dislocation density and orientation close to the parent grain orientation. This is illustrated in figure 6, which shows clusters of small grains all over the grain boundaries. The pole figure in figure 6*b* shows the grain orientations with a colourscale related to the GOS value of the grain. The size of the symbol is proportional to the

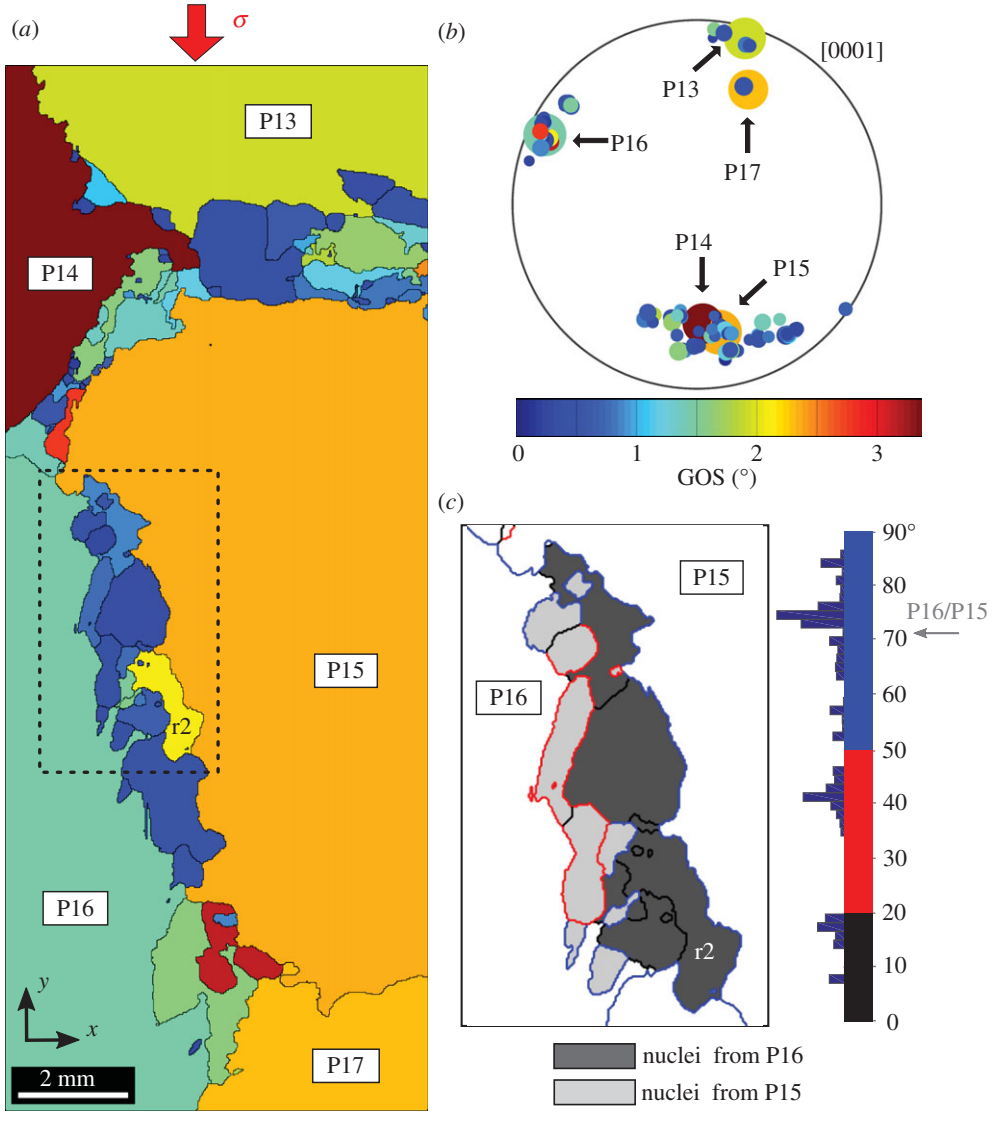

Figure 6. (*a*) EBSD map (20 µm step size) using GOS colour-coding. The grain boundaries are plotted in black (misorientation angle higher than 7°). (*b*) *c*-Axis pole figure using GOS colour-coding and a maker size proportional to the grain size. (*c*) Map of the dashed rectangular area. The nuclei are coloured depending on the inferred 'parent' grain P15 or P16. The grain boundaries are colour-coded using the misorientation angle. The frequency histogram of the misorientation angle boundaries is added to the colour-bar and the initial misorientation between P15 and P16 is shown by the arrow. (Online version in colour.)

size of the grain allowing one to distinguish small (possible nuclei) from large grains (parents). It appears that all new grains cluster around an orientation very close to the orientation of one of the large grains in the domain. The larger misorientation measured between a nucleus and its parent grain is about 30° (relative to grains P14 and P15). Although most of these new grains have low GOS values, some show higher GOS values suggesting that they either represent new grains that started to deform during the test or are residues from parent grains isolated by nuclei growth (as could be the case of r1 in figure 5).

Figure 6*c* focuses on the small grains along the grain boundary between grains P15 and P16 (P15/P16). The grains are colour-coded depending on the parent from which they are supposed to originate (P15 or P16) based on their orientation. The representation of the grain boundaries

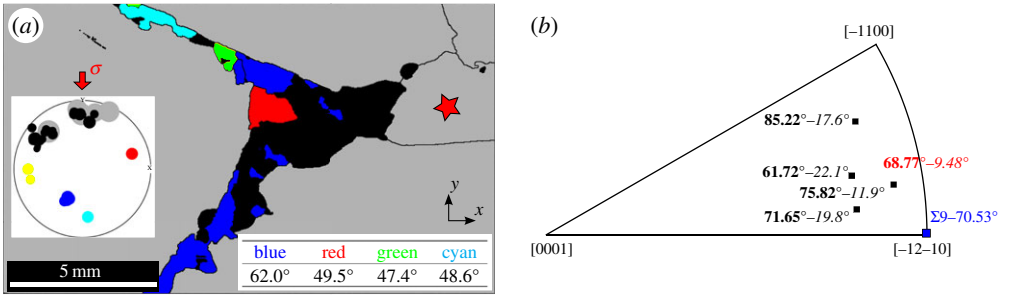

Figure 7. (*a*) EBSD colour map and pole figure colour-coded depending on the 'nature' of the grain. The grains inherited from the initial sample appear in grey. The nuclei formed by bulging appear in black. The nuclei with new orientations appear in blue, cyan, green and red. The table provides the misorientation angle between the new small grains and the closest parent grains (grey). The grain boundaries are plotted in black (misorientation angle higher than 7°). (*b*) Theoretical coincidence site lattice (CSL) for Ice-Ih [62] and the misorientation axes between the blue nuclei and the five neighbouring grains. The associated misorientation angle is in bold and the misorientation angle between the rotation axis and the closest CSL rotation axis in italics. The red misorientation axis corresponds to the misorientation axis between the blue grain and the grain marked by the red star. (Online version in colour.)

is a function of the misorientation. Grain boundaries with misorientations between 7° and 20° are shown in black and those between 20° and 50°, in red. Grain boundaries with misorientation angle between 50° and 90° (i.e. close to the initial grain boundary P15/P16 misorientation 70° ± 20°) are depicted in blue. The grain boundaries with low angle or similar to the initial P15/P16 misorientation are those expected to have formed by bulging. The intermediate grain boundary misorientation (red) might result from bulging of an 'old' nuclei.

It is interesting to note that the dispersion of the orientation of the *c*-axis of the nuclei around grain P15 is larger than the one of the nuclei around grain P16 (figure 6*b*). Moreover, the nuclei emanating from P16 seem to present higher GOS values than the ones from P15, as for instance grain r2 which could very likely be a remnant of grain P16. These observations indicate that the nuclei likely grew from grain P15 into grain P16 at this location along the boundary.

In summary, bulging seems to be an efficient nucleation mechanism in this study (figure 1). It creates necklace structures along the original grain boundaries.

(ii) Nucleation with no orientation relation with parent grains

A few locations in the samples analysed in this study suggest the occurrence of a nucleation mechanism that induces no orientation relation between the nucleus and the parent grains. This type of nucleation was hypothesized by Duval *et al.* [23] to result from a 'spontaneous' nucleation mechanism with neither critical radius nor saddle point energy constraint.

One of these locations is represented in figure 7*a*. In order to highlight the orientation data, grains within this area are colour-coded as a function of their orientation. Grey is used for grains initially present in the undeformed microstructure (parent grains). Small grains with orientations close to one of the parent grains are coloured in black. They are interpreted as resulting from bulging, as described in §3b(i). The remaining small grains are coloured based on their orientation, as in the pole figure (figure 7*a*). They show orientations that differ significantly from the parent grain orientation (table in figure 7*a*). For instance, the blue grain is misoriented by 62.0° from the closest possible parent grain, while the maximum misorientation angle in a hexagonal system is 93.8°.

Twinning, which would result in coincidence site lattice (CSL) orientation relations, was excluded based on the relations of orientation (figure 7*b*). Indeed, from theoretical CSL in ice estimated by Gonzalez Kriegel *et al.* [62], the misorientation between a nucleus and the parents that gets the closest to a CSL ($\Sigma 9$ CSL [62]) corresponds to a rotation axis that stands at about 10° from the $\Sigma 9$ CSL configuration expected for ice.

Could orientation relations exist in the third dimension which is not resolved by our EBSD surface observations? This cannot be totally excluded, but it is very unlikely considering the columnar shape and the large initial grain size. Nevertheless, the nucleation destroys the 2.5-dimensional symmetry of the original microstructure, and the small blue grains could well be part of one single larger grain (resulting from nucleation and growth) cut by the surfacing procedure.

4. Discussion

Ice deformation is mainly accommodated by dislocation glide along the basal plane. Owing to the difficulty of propagation of non-basal dislocations, ice single crystals have strong anisotropic mechanical properties [1]. This strong anisotropy leads to heterogeneous strain fields during deformation of ice polycrystals [20]. Locally, at an intra-granular scale or within deformation bands, the strain can be more than ten times higher than the macroscopic strain [3,20]. Close to grain boundaries, where strain incompatibility is stronger, strain localization is a precursor to recrystallization mechanisms [3], as a response to stress heterogeneity [21,22]. The role of recrystallization mechanisms is to reduce these heterogeneities through grain nucleation, SGB formation and grain boundary migration, by creating a more strain compatible microstructure [3].

Kink bands are common sub-structures in ice, as described in [32,63]. Piazolo *et al.* [22] have recently shown that they accommodate strong local stresses resulting from strain incompatibility and compensate the difficulty of non-basal dislocation glide. The kink interior can be rotated by a few degrees relative to the surrounding grain (figure 2), favouring the glide of basal dislocations. The local deformation accommodated by a kink band may be important, as recently evaluated by digital image correlation on ice [3].

This study details many examples of kink band structures (figure 2). It shows, for the first time, that the tilt SGBs forming the kink bands do not necessarily take the shape of a sharp wall. Although rare, progressive misorientations may also occur. Multiple layers of basal edge dislocations parallel to the tilt SGBs are needed to create such a structure. Some kink bands crosscut the entire grain and create new path to accommodate the deformation imposed by the local stress field. Kink band sub-structures are however more numerous close to grain boundaries than within the grain (figure 2*c*). This is consistent with the fact that the strain incompatibilities are stronger close to grain boundaries. When going deeper into the grains, the sub-structures therefore tend to arrange in simpler shapes with reduced stored energy.

Isolated tilt SGBs and multiple tilt SGBs that result in progressive bending of the crystal lattice (electronic supplementary material), or more complex mosaic sub-structures formed by multiple tilt SGBs (grain P8, figure 3) are also frequently observed in our samples. All these sub-structures may be formed by basal edge dislocations such as already hypothesized in [29,30].

Development of SGBs as observed in this study (tilt SGB, kink band, etc.) creates distinct sub-grains that can be misoriented by a few degrees (figure 3 for instance). The arbitrary value of 7° assigned here to distinguish between SGB and grain boundary is based on empirical observations of various authors (see for instance [41]), but not supported by any energy calculation, as shown in part 2 of the electronic supplementary material. SGBs observed in this study or in natural ice cores [29,31] do not organize in a type of checkerboard as in halite [64,65], quartz [66] or in magnesium [67,68]. Most often, the SGBs crosscut the entire grain and separate large parts of grains into well-defined sub-grains that further behave as individual grains [3]. These mechanisms can be interpreted as continuous DRX because they end up creating distinct grains.

Grain boundary bulging has been proposed as an efficient recrystallization mechanism for ice in previous studies, based on observation of ice core samples [31] or laboratory experiments [19]. For the first time, this study uses original cryo-EBSD observations at relatively high resolution to provide a description of the different steps of nucleation by bulging, from the serrated grain boundary to the new small grain (figures 4–6).

Observed grain boundary serrations result from SIBM [49,69] and this heterogeneous migration is associated with complex crystal sub-structures close to the grain boundary (figure 4). These sub-structures are shown here to be mostly tilt SGBs with basal $\langle a \rangle$ edge dislocations but

a non-negligible proportion of them contains non-basal ⟨*c*⟩ dislocations (figure 4) that appear necessary to complete the sub-grains. Although the role of such energetically unfavourable dislocations [2] in forming dislocation sub-structures has already been evoked by Weikusat *et al.* [29] and Piazolo *et al.* [22], they appear, here, to be very common close to serrated grain boundaries. As such SGBs containing non-basal dislocations are expected to be energetically costly in ice, they might require high levels of local stresses such as can be expected close to grain boundaries and triple junctions [20,22].

From our observations, it is very likely that these complex SGBs will actively contribute to the isolation of the nuclei with increasing strain (nuclei *n*1 and *n*2, figure 5). Nuclei created by bulging have a low dislocation density and seem to grow in the direction where the dislocation density is higher. Their nucleation that occurs along old grain boundaries may result in the development of a necklace of small grains at grain boundaries (figure 6) as frequently observed in metals [70] or in minerals [71].

Bulging nucleation is observed in metals such as magnesium [46,72,73], copper [44,74] and in rocks [47,69,75], where it is supposed to be responsible for a drastic grain size decrease during discontinuous DRX. In the specific conditions of our experiments (high temperature, high deviatoric stress), grain boundary migration is supposed to dominate the grain microstructure evolution [19], and we therefore expect new strain free grains to grow rapidly.

Polygonization associated with tilt SGBs or kink bands, or nucleation by bulging are expected to create new grains with orientations close to the ones of parent grains [49,76]. Small grains with an orientation that did not exist in the initial microstructure are also observed in this study (figure 7). These new small grains, observed in figure 7, present high angle grain boundaries with no CSL relationship with the neighbouring grains. Similar observations were performed in metals under conditions where discontinuous DRX is expected to dominate [77–79].

Along deep ice cores, where the texture is close to a single maximum aligned with the vertical axis (compression direction), some isolated grains are observed whose orientations clearly stand out of the dominant orientation cluster at the given depth [15,16]. Discontinuous DRX has been suggested as an explanation for these isolated orientations but no physical mechanism was evoked [4].

The model suggested by Duval *et al.* [23] could provide a likely explanation for the formation of such nuclei. This model proposes that the relaxation, during embryo formation, of long-range internal stresses stored in dislocation pile-ups at grain boundaries provides an additional driving force that drastically decreases both the nucleation critical radius and the saddle point energy. In these conditions, nucleation can occur without the necessity to reach a critical nucleus size [80], nor any thermal activation. This is why is it referred to as 'spontaneous' nucleation. The critical strain necessary to establish the long-range internal stress field is probably achieved thanks to the strong localization of deformation in ice, due to incompatibilities between grains. Although this model does not constrain the nucleus orientation, it may explain new orientations that appear with no relation to the parent grains.

Dynamic recrystallization in ice involves complex crystal restructuring through various forms of nucleation. As shown during a previous study [3], these mechanisms are a response to the incompatibility of deformation between grains and create new microstructures more compatible in regard to the local stress. Nucleation mechanisms observed during laboratory experiments (for instance here $T = -7^{\circ}\mathrm{C}$ and $\sigma = 0.5\,\mathrm{MPa}$) can take various forms within a single sample, indicating concomitant activation of both continuous DRX and discontinuous DRX. The local strain and stress fields very likely control which mechanism predominates, which one is the most efficient to relax the local incompatibilities. The macroscopic stress and strain conditions impose nevertheless the global textures that form in conditions of DRX in ice [18,19,81,82]. We can therefore expect nucleation mechanisms to provide the evolution of the microstructure required to achieve a macroscopically favourable state of stress. Macroscopic deformation bands as observed in [20] might be favourable sites of nucleation.

While laboratory conditions ($\dot{\varepsilon} \sim 10^{-7}\,\mathrm{s}^{-1}$) are far from the deformation conditions encountered in natural ice sheets ($\dot{\varepsilon} \sim 10^{-12}\,\mathrm{s}^{-1}$), the extraordinarily strong viscoplastic

anisotropy of ice [1] and the complex substructures visible in natural samples [31] even at high depths in the firn [83] suggest that strain heterogeneities can be strong in natural conditions too. As strain rate in ice sheets is several orders of magnitude lower than in laboratory conditions, we expect grain boundary migration to have a stronger relative impact on the relaxation of local stresses during deformation. This is coherent with the observed grain shapes, which are less serrated in natural samples [31]. However, the local stresses are probably still high enough to create SGBs with basal edge dislocations but also SGBs with non-basal dislocations [29]. Yet, discontinuous DRX cannot be considered as the dominant mechanism at all depths in an ice sheet. First of all, and mostly, because observed textures along the first two-thirds of most of the cores present a single maximum [7,8,15,16] that strongly differs from the 'small circles'-type textures observed in all creep experiments in DRX conditions [18,19,82], while in the bottom part of ice cores the textures become similar to the experimental ones [6,8,17]. The increase in temperature with depth along ice cores is likely to modify the balance between grain boundary migration rate and storage of strain energy through dislocation accumulation. The shear component of stress also increases with depth in an ice sheet [11,84,85]. This could induce higher strain heterogeneities and hence more effective recrystallization. At these lower depths grain sizes can also be very large, in agreement with an efficient grain boundary migration.

Evaluating the mechanisms of nucleation in the laboratory and at a relatively high resolution is therefore likely to benefit to the understanding of DRX mechanisms as occurring along ice cores. High resolution observations of ice samples extracted from ice core, such as performed by Weikusat *et al.* [31], could be valuable to perform comparisons. Nevertheless, as many bubbles are trapped in ice, and compressed in their natural environment, their relaxation with ice extraction can lead to severe local deformation at the intragranular scale that will very likely pollute EBSD observations of local dislocation sub-structures.

5. Conclusion

In this study, cryo-EBSD observations on columnar ice deformed at high temperature provide a detailed overview of the nucleation processes occurring during DRX of ice and of the likely associated dislocation arrangements.

Nucleation mechanisms in a strong anisotropic material such as ice are mainly controlled by the local strain and stress conditions. These conditions are strongly heterogeneous and high local strains can be reached at any macroscopic strain level [3,20]. Nucleation and grain boundary migration are efficient mechanisms to accommodate the intra- and intergranular stress incompatibilities by creating a new microstructure more adapted to the local stress field. This study highlights the range of nucleation mechanisms that can act to modify the microstructure, as a function of the local and macroscopic constraints.

Most commonly, dislocations organize to form tilt SGBs and kink bands which accommodate significant strain [3] at places where local stress is heterogeneous [22]. Although no '*in situ*' observations are available, it is very likely from the present observations that these dislocation sub-structures can be considered as precursors to a polygonization type of nucleation.

For the first time, bulging nucleation is characterized in detail. SGBs are shown to play a major role in this nucleation associated with strain induced grain boundary migration. Indeed, strongly misoriented areas concentrate close to serrated grain boundaries. These areas contain classical tilt bands made of basal dislocations, but also of non-basal dislocations. These sub-structures, which must be driven by high local stress concentrations, are very likely to be responsible for evolution of the bulging nuclei into new grains that are observed in this study, although only *in situ* experiments could undoubtedly provide the proof. Local and heterogeneous grain boundary migration, exemplified by serrated grain boundaries, enables microstructure restructuration adapted to the local fields. But our observations demonstrate that the classical scheme of 'strain free' grains that would grow against 'highly strained' grains is far too simplistic in a frame of heterogeneous strain field such as measured in ice.

'Spontaneous' nucleation was also deduced from observation of necklaces of small grains at grain boundaries and triple junctions with no orientation relation with parent grain. Although indirect, this observation is the first one that could validate the model of Duval *et al.* [23] of a 'spontaneous' nucleation resulting from the impact of dislocation induced internal stress field. Such a mechanism could be evoked to explain abrupt changes in texture along ice cores, from strong single maximum to dispersed texture as observed by Montagnat *et al.* [16] for instance.

The detailed and unique observations performed in this work challenge the classical separation between 'continuous' and 'discontinuous' DRX in the case of a material with a strong viscoplastic anisotropy deformed at high temperature, because nucleation mechanisms associated with both regimes are observed simultaneously. The extrapolation of these observations to the dominant recrystallization mechanisms in ice sheet conditions and their impact on texture development is still challenging, but the role of strain and stress heterogeneities is likely to be important, even at low strain rates.

Authors' contributions. T.C. carried out the experiments. T.C., F.B., K.H., M.M. and A.T. carried out the EBSD measurements. T.C. and D.M. developed tools for data treatment. T.C. and M.M. wrote the paper. All authors participated to the interpretation of the experiments. All authors corrected and approved the manuscript.

Competing interests. The authors declare that they have no competing interests.

Funding. Financial support by the French Agence Nationale de la Recherche is acknowledged (project DREAM, no. ANR-13-BS09-0001-01). This work benefited from support from institutes INSIS and INSU of CNRS. It has been supported by a grant from Labex OSUG@2020 (ANR10 LABX56). This project is supported by INP-Grenoble and the University Joseph Fourier in the frame of proposal called 'Grenoble Innovation Recherche AGIR'. This project is supported by Marie Curie Intra-European Fellowship (PIEF-GA-2012-327226).

Acknowledgements. Many thanks to Paul Duval for long-term useful discussions and comments.

References

1. Duval P, Ashby MF, Anderman I. 1983 Rate-controlling processes in the creep of polycrystalline ice. *J. Phys. Chem.* **87**, 4066–4074. (doi:10.1021/j100244a014)
2. Hondoh T. 2000 Nature and behavior of dislocations in ice. In *Physics of ice core records*, pp. 3–23. Sapporo, Japan: Hokkaido University Press.
3. Chauve T, Montagnat M, Vacher P. 2015 Strain field evolution during dynamic recrystallization nucleation; a case study on ice. *Acta Mater.* **101**, 116–124. (doi:10.1016/j.actamat.2015.08.033)
4. Montagnat M, Durand G, Duval P. 2009 Recrystallization processes in granular ice. *Low Temperature Sci.* **68**, 81–90.
5. Wilson CJ, Peternell M, Piazolo S, Luzin V. 2013 Microstructure and fabric development in ice: lessons learned from *in situ* experiments and implications for understanding rock evolution. *J. Struct. Geol.* **61**, 50–77. (doi:10.1016/j.jsg.2013.05.006)
6. De La Chapelle S, Castelnau O, Lipenkov V, Duval P. 1998 Dynamic recrystallization and texture development in ice as revealed by the study of deep ice cores in Antarctica and Greenland. *J. Geophys. Res. Solid Earth* **103**, 5091–5105. (doi:10.1029/97JB02621)
7. Lipenkov VY, Barkov NI, Dural P, Pimenta P. 1989 Crystalline texture of the 2083 m ice core at Vostok Station, Antarctica. *J. Glaciol.* **35**, 392–398
8. Thorsteinsson T, Kipfstuhl J, Miller H. 1997 Textures and fabrics in the GRIP ice core. *J. Geophys. Res.* **102**, 26 583–26 599. (doi:10.1029/97JC00161)
9. Castelnau O, Thorsteinsson T, Kipfstuhl J, Duval P, Canova GR. 1996 Modelling fabric development along the GRIP ice core, central Greenland. *Ann. Glaciol.* **23**, 194–201. (doi:10.3198/1996AoG23-194-201)
10. Gillet-Chaulet F. 2006 Modélisation de l'écoulement de la glace polaire anisotrope et premières applications au forage de Dôme C. PhD thesis, Université Joseph-Fourier-Grenoble I, France.
11. Durand G, Gillet-Chaulet F, Svensson A, Gagliardini O, Kipfstuhl S, Meyssonnier J, Parrenin F, Duval P, Dahl-Jensen D. 2007 Change in ice rheology during climate variations—implications for ice flow modelling and dating of the EPICA Dome C core. *Clim. Past* **3**, 155–167. (doi:10.5194/cp-3-155-2007)

12. Alley RB, Gow AJ, Meese DA. 1995 Mapping c-axis fabrics to study physical processes in ice. *J. Glaciol.* **41**, 197–203.
13. Durand G, Persson A, Samyn D, Svensson A. 2008 Relation between neighbouring grains in the upper part of the *NorthGRIP* ice core—implications for rotation recrystallization. *Earth Planet. Sci. Lett.* **265**, 666–671. (doi:10.1016/j.epsl.2007.11.002)
14. Gow AJ, Williamson T. 1976 Rheological implications of the internal structure and crystal fabrics of the West Antarctic ice sheet as revealed by deep core drilling at Byrd Station. *Geological Soc. Am. Bull.* **87**, 1665–1677. (doi:10.1130/0016-7606(1976)87<1665:RIOTIS>2.0.CO;2)
15. Durand G, Svensson A, Persson A, Gagliardini O, Gillet-Chaulet F, Sjolte J, Montagnat M, Dahl-Jensen D. 2009 Evolution of the texture along the EPICA dome C ice core. *Low Temperature Sci.* **68**, 91–106.
16. Montagnat M, Buiron D, Arnaud L, Broquet A, Schlitz P, Jacob R, Kipfstuhl S. 2012 Measurements and numerical simulation of fabric evolution along the Talos Dome ice core, Antarctica. *Earth Planet. Sci. Lett.* **357–358**, 168–178. (doi:10.1016/j.epsl.2012.09.025)
17. Diprinzio CL, Wilen LA, Alley RB, Fitzpatrick JJ, Spencer MK, Gow AJ. 2005 Fabric and texture at Siple Dome, Antarctica. *J. Glaciol.* **51**, 281–290. (doi:10.3189/172756505781829359)
18. Jacka T, Maccagnan M. 1984 Ice crystallographic and strain rate changes with strain in compression and extension. *Cold Regions Sci. Technol.* **8**, 269–286. (doi:10.1016/0165-232X(84)90058-2)
19. Montagnat M, Chauve T, Barou F, Tommasi A, Beausir B, Fressengeas C. 2015 Analysis of dynamic recrystallization of ice from EBSD orientation mapping. *Front. Earth Sci.* **3**, 81. (doi:10.3389/feart.2015.00081)
20. Grennerat F, Montagnat M, Castelnau O, Vacher P, Moulinec H, Suquet P, Duval P. 2012 Experimental characterization of the intragranular strain field in columnar ice during transient creep. *Acta Mater.* **60**, 3655–3666. (doi:10.1016/j.actamat.2012.03.025)
21. Montagnat M, Blackford JR, Piazolo S, Arnaud L, Lebensohn RA. 2011 Measurements and full-field predictions of deformation heterogeneities in ice. *Earth Planet. Sci. Lett.* **305**, 153–160. (doi:10.1016/j.epsl.2011.02.050)
22. Piazolo S, Montagnat M, Grennerat F, Moulinec H, Wheeler J. 2015 Effect of local stress heterogeneities on dislocation fields: examples from transient creep in polycrystalline ice. *Acta Mater.* **90**, 303–309. (doi:10.1016/j.actamat.2015.02.046)
23. Duval P, Louchet F, Weiss J, Montagnat M. 2012 On the role of long-range internal stresses on grain nucleation during dynamic discontinuous recrystallization. *Mater. Sci. Eng. A* **546**, 207–211. (doi:10.1016/j.msea.2012.03.052)
24. Glen JW, Perutz MF. 1954 The growth and deformation of ice crystals. *J. Glaciol.* **2**, 397–403. (doi:10.3189/002214354793702434)
25. Shearwood C, Whitworth RW. 1989 X-ray topographic observations of edge dislocation glide on non-basal planes in ice. *J. Claciol.* **35**, 281–283. (doi:10.3198/1989JoG35-120-281-283)
26. Shearwood C, Whitworth RW. 1991 The velocity of dislocations in ice. *Philos. Mag. A* **64**, 289–302. (doi:10.1080/01418619108221186)
27. Hondoh T, Anzai H, Goto A, Mae S, Higashi A, Langway Jr CC. 1990 The crystallographic structure of the natural air-hydrate in Greenland dye-3 deep ice core. *J. Inclusion Phenomena Mol. Recognition Chem.* **8**, 17–24. (doi:10.1007/BF01131284)
28. Louchet F. 2004 A model for steady state plasticity of ice single crystals. *Philos. Mag. Lett.* **84**, 797–802. (doi:10.1080/09500830500071507)
29. Weikusat I, Miyamoto A, Faria SH, Kipfstuhl S, Azuma N, Hondoh T. 2011 Subgrain boundaries in Antarctic ice quantified by X-ray Laue diffraction. *J. Glaciol.* **57**, 111–120. (doi:10.3189/002214311795306628)
30. Piazolo S, Montagnat M, Blackford JR. 2008 Sub-structure characterization of experimentally and naturally deformed ice using cryo-EBSD. *J. Microsc.* **230**, 509–519. (doi:10.1111/j.1365-2818.2008.02014.x)
31. Weikusat I, Kipfstuhl S, Faria SH, Azuma N, Miyamoto A. 2009 Subgrain boundaries and related microstructural features in EDML (Antarctica) deep ice core. *J. Glaciol.* **55**, 461–472. (doi:10.3189/002214309788816614)
32. Wilson CJL, Burg JP, Mitchell JC. 1986 The origin of kinks in polycrystalline ice. *Tectonophysics* **127**, 27–48. (doi:10.1016/0040-1951(86)90077-6)

33. Barsoum MW, Radovic M, Finkel P, El-Raghy T. 2001 Ti_3SiC_2 and ice. *Appl. Phys. Lett.* **79**, 479–481. (doi:10.1063/1.1384479)
34. Aydiñer CC, Telemez MA. 2014 Multiscale deformation heterogeneity in twinning magnesium investigated with in situ image correlation. *Int. J. Plast.* **56**, 203–218. (doi:10.1016/j.ijplas.2013.12.001)
35. Hazeli K, Cuadra J, Streller F, Barr C, Taheri M, Carpick R, Kontsos A. 2015 Three-dimensional effects of twinning in magnesium alloys. *Scripta Mater.* **100**, 9–12. (doi:10.1016/j.scriptamat.2014.12.001)
36. Hama T, Nagao H, Kobuki A, Fujimoto H, Takuda H. 2015 Work-hardening and twinning behaviors in a commercially pure titanium sheet under various loading paths. *Mater. Sci. Eng. A* **620**, 390–398. (doi:10.1016/j.msea.2014.10.024)
37. Burkhard M. 1993 Calcite twins, their geometry, appearance and significance as stress-strain markers and indicators of tectonic regime: a review. *J. Struct. Geol.* **15**, 351–368. (doi:10.1016/0191-8141(93)90132-T)
38. Yamasaki M, Hagihara K, Inoue Si, Hadorn JP, Kawamura Y. 2013 Crystallographic classification of kink bands in an extruded Mg–Zn–Y alloy using intragranular misorientation axis analysis. *Acta Mater.* **61**, 2065–2076. (doi:10.1016/j.actamat.2012.12.026)
39. Galiyev A, Kaibyshev R, Sakai T. 2003 Continuous dynamic recrystallization in magnesium alloy. *Mater. Sci. Forum* **419–422**, 509–514. (doi:10.4028/www.scientific.net/MSF.419-422.509)
40. Sakai T, Miura H, Goloborodko A, Sitdikov O. 2009 Continuous dynamic recrystallization during the transient severe deformation of aluminum alloy 7475. *Acta Mater.* **57**, 153–162. (doi:10.1016/j.actamat.2008.09.001)
41. Drury MR, Urai JL. 1990 Deformation-related recrystallization processes. *Tectonophysics* **172**, 235–253. (doi:10.1016/0040-1951(90)90033-5)
42. Trimby PW, Drury MR, Spiers CJ. 2000 Recognising the crystallographic signature of recrystallisation processes in deformed rocks: a study of experimentally deformed rocksalt. *J. Struct. Geol.* **22**, 1609–1620. (doi:10.1016/S0191-8141(00)00059-6)
43. Trepmann CA, Renner J, Druiventak A. 2013 Experimental deformation and recrystallization of olivine—processes and timescales of damage healing during postseismic relaxation at mantle depths. *Solid Earth* **4**, 423–450. (doi:10.5194/se-4-423-2013)
44. Ito T, Taketani T, Nakayama Y. 1986 Dynamic recrystallization by the bulging of grain boundaries in polycrystalline dilute copper alloys. *Scripta Metall.* **20**, 1329–1332. (doi:10.1016/0036-9748(86)90089-X)
45. McDonald DT, Humphreys JF, Bate PS. 2005 Nucleation and texture development during dynamic recrystallization of copper. *Mater. Sci. Forum* **495**, 1195–1200. (doi:10.4028/www.scientific.net/MSF.495-497.1195)
46. Galiyev A, Kaibyshev R, Gottstein G. 2001 Correlation of plastic deformation and dynamic recrystallization in magnesium alloy ZK60. *Acta Mater.* **49**, 1199–1207. (doi:10.1016/S1359-6454(01)00020-9)
47. Rutter EH. 1995 Experimental study of the influence of stress, temperature, and strain on the dynamic recrystallization of Carrara marble. *J. Geophys. Res. Solid Earth* **100**, 24 651–24 663. (doi:10.1029/95JB02500)
48. Duval P, Castelnau O. 1995 Dynamic recrystallization of ice in polar ice sheets. *Le J. de Phys. IV* **05**, C3-197–C3-205.
49. Humphreys FJ, Hatherly M. 2004 *Recrystallization and related annealing phenomena*, 2nd edn. Oxford, UK: Pergamon.
50. Plé O, Meyssonnier J. 1997 Preparation and preliminary study of structure-controlled S2 columnar ice. *J. Phys. Chem. B* **101**, 6118–6122. (doi:10.1021/jp963256t)
51. Russell-Head D, Wilson CJL. 2001 Automated fabric analyser system for quartz and ice. In *Geological Society of Australia Abstracts*, vol. 64, pp. 159–159. Hornsby, Australia: Geological Society of Australia.
52. Peternell M, Russell-Head D, Wilson CJL. 2011 A technique for recording polycrystalline structure and orientation during in situ deformation cycles of rock analogues using an automated fabric analyser. *J. Microsc.* **242**, 181–188. (doi:10.1111/j.1365-2818.2010.03456.x)
53. Randle V. 1992 *Microtexture determination and its applications*, p. 174. London, UK: The Institute of Materials.

54. Weikusat I, De Winter DAM, Pennock GM, Hayles M, Schneijdenberg C, Drury MR. 2011 Cryogenic EBSD on ice: preserving a stable surface in a low pressure SEM. *J. Microsc.* **242**, 295–310. (doi:10.1111/j.1365-2818.2010.03471.x)
55. Bachmann F, Hielscher R, Schaeben H. 2010 Texture analysis with MTEX—free and open source software toolbox. *Solid State Phenomena* **160**, 63–68. (doi:10.4028/www.scientific.net/SSP.160.63)
56. Suzuki S. 1970 Grain coarsening of microcrystals of ice (III). *Low Temp. Sci. Ser. A* **28**, 47–61.
57. Petrenko VF, Whitworth RW. 1999 *Physics of ice*. Oxford, UK: Clarendon Press.
58. Read WT, Shockley W. 1950 Dislocation models of crystal grain boundaries. *Phys. Rev.* **78**, 275–289. (doi:10.1103/PhysRev.78.275)
59. Prior DJ, Wheeler J, Peruzzo L, Spiess R, Storey C. 2002 Some garnet microstructures: an illustration of the potential of orientation maps and misorientation analysis in microstructural studies. *J. Struct. Geol.* **24**, 999–1011. (doi:10.1016/S0191-8141(01)00087-6)
60. Friedel J. 1964 *Dislocations*, vol. 70, pp. 15–24. Oxford, UK: Pergamon Press.
61. Urai J, Means W, Lister G. 1986 Dynamic recrystallization of minerals. In *Mineral and rock deformation: laboratory studies* (eds BE Hobbs, HC Heard). Geophysical Monograph, pp. 161–200.
62. Gonzalez Kriegel BJ, Di Prinzio CL, Nasello OB. 1997 Exact coincidence site lattice in ice Ih. *J. Phys. Chem. B* **101**, 6243–6246. (doi:10.1021/jp9632753)
63. Mansuy P, Philip A, Meyssonnier J. 2000 Identification of strain heterogeneities arising during deformation of ice. *Ann. Glaciol.* **30**, 121–126. (doi:10.3189/172756400781820651)
64. Guillope M, Poirier JP. 1979 Dynamic recrystallization during creep of single-crystalline halite: an experimental study. *J. Geophys. Res. Solid Earth* **84**, 5557–5567. (doi:10.1029/JB084iB10p05557)
65. Drury M, Pennock G. 2007 Subgrain rotation recrystallization in minerals. *Mater. Sci. Forum* **550**, 95–104. (doi:10.4028/www.scientific.net/MSF.550.95)
66. Stipp M, Stünitz H, Heilbronner R, Schmid SM. 2002 The eastern Tonale fault zone: a 'natural laboratory' for crystal plastic deformation of quartz over a temperature range from 250 to 700°C. *J. Struct. Geol.* **24**, 1861–1884. (doi:10.1016/S0191-8141(02)00035-4)
67. Tan JC, Tan MJ. 2003 Dynamic continuous recrystallization characteristics in two stage deformation of Mg-3Al-1Zn alloy sheet. *Mater. Sci. Eng. A* **339**, 124–132. (doi:10.1016/S0921-5093(02)00096-5)
68. Fatemi-Varzaneh SM, Zarei-Hanzaki A, Cabrera JM, Calvillo PR. 2015 EBSD characterization of repetitive grain refinement in AZ31 magnesium alloy. *Mater. Chem. Phys.* **149–150**, 339–343. (doi:10.1016/j.matchemphys.2014.10.026)
69. Prior DJ, Bestmann M, Halfpenny A, Mariani E, Piazolo S, Tullis J, Wheeler J. 2004 Recrystallization and grain growth in rocks and minerals. *Mater. Sci. Forum* **467–470**, 545–550. (doi:10.4028/www.scientific.net/MSF.467-470.545)
70. Ponge D, Gottstein G. 1998 Necklace formation during dynamic recrystallization: mechanisms and impact on flow behavior. *Acta Mater.* **46**, 69–80. (doi:10.1016/S1359-6454(97)00233-4)
71. Halfpenny A, Prior DJ, Wheeler J. 2006 Analysis of dynamic recrystallization and nucleation in a quartzite mylonite. *Tectonophysics* **427**, 3–14. (doi:10.1016/j.tecto.2006.05.016)
72. Ihara K, Miura Y. 2004 Dynamic recrystallization in Al-Mg-Sc alloys. *Mater. Sci. Eng. A* **387–389**, 647–650. (doi:10.1016/j.msea.2004.05.082)
73. Fatemi-Varzaneh SM, Zarei-Hanzaki A, Beladi H. 2007 Dynamic recrystallization in AZ31 magnesium alloy. *Mater. Sci. Eng. A* **456**, 52–57. (doi:10.1016/j.msea.2006.11.095)
74. Wusatowska-Sarnek AM, Miura H, Sakai T. 2002 Nucleation and microtexture development under dynamic recrystallization of copper. *Mater. Sci. Eng. A* **323**, 177–186. (doi:10.1016/S0921-5093(01)01336-3)
75. Platt JP, Behr WM. 2011 Grainsize evolution in ductile shear zones: implications for strain localization and the strength of the lithosphere. *J. Struct. Geol.* **33**, 537–550. (doi:10.1016/j.jsg.2011.01.018)
76. Sakai T, Belyakov A, Kaibyshev R, Miura H, Jonas JJ. 2014 Dynamic and post-dynamic recrystallization under hot, cold and severe plastic deformation conditions. *Prog. Mater. Sci.* **60**, 130–207. (doi:10.1016/j.pmatsci.2013.09.002)
77. Humphreys FJ. 2004 Nucleation in recrystallization. *Mater. Sci. Forum* **467–470**, 107–116. (doi:10.4028/www.scientific.net/MSF.467-470.107)

78. Larsen AW, Poulsen HF, Margulies L, Gundlach C, Xing Q, Huang X, Jensen DJ. 2005 Nucleation of recrystallization observed in situ in the bulk of a deformed metal. *Scripta Mater.* **53**, 553–557. (doi:10.1016/j.scriptamat.2005.04.053)
79. Wu GL, Juul Jensen D. 2007 Orientations of recrystallization nuclei developed in columnar-grained Ni at triple junctions and a high-angle grain boundary. *Acta Mater.* **55**, 4955–4964. (doi:10.1016/j.actamat.2007.05.019)
80. Brechet Y, Martin G. 2006 Nucleation problems in metallurgy of the solid state: recent developments and open questions. *C. R. Phys.* **7**, 959–976. (doi:10.1016/j.crhy.2006.10.014)
81. Bouchez JL, Duval P. 1982 The fabric of polycrystalline ice deformed in simple shear: experiments in torsion, natural deformation and geometrical interpretation. *Textures Microstruct.* **5**, 171–190. (doi:10.1155/TSM.5.171)
82. Treverrow A, Budd WF, Jacka TH, Warner RC. 2012 The tertiary creep of polycrystalline ice: experimental evidence for stress-dependent levels of strain-rate enhancement. *J. Glaciol.* **58**, 301–314. (doi:10.3189/2012JoG11J149)
83. Kipfstuhl S, Faria SH, Azuma N, Freitag J, Hamann I, Kaufmann P, Miller H, Weiler K, Wilhelms F. 2009 Evidence of dynamic recrystallization in polar firn. *J. Geophys. Res.* **114**, B05204. (doi:10.1029/2008JB005583)
84. Paterson WSB. 1994 *The physics of glaciers*. Oxford, UK: Pergamon.
85. Montagnat M *et al.* 2014 Multiscale modeling of ice deformation behavior. *J. Struct. Geol.* **61**, 78–108. (doi:10.1016/j.jsg.2013.05.002)